Ion and inhibitor binding of the double-ring ion selectivity filter of the mitochondrial calcium uniporter

Chan Cao[a,b], Shuqing Wang[c], Tanxing Cui[a], Xun-Cheng Su[b,1], and James J. Chou[a,d,1]

[a]Department of Biological Chemistry and Molecular Pharmacology, Harvard Medical School, Boston, MA 02115; [b]State Key Laboratory of Elemento-Organic Chemistry, Collaborative Innovation Center of Chemical Science and Engineering (Tianjin), Nankai University, Tianjin 300071, China; [c]School of Pharmacy, Tianjin Medical University, Tianjin 300070, China; and [d]State Key Laboratory of Molecular Biology, National Center for Protein Science Shanghai, Shanghai Institute of Biochemistry and Cell Biology, Shanghai Science Research Center, Chinese Academy of Sciences, Shanghai 200031, China

Edited by Christopher Miller, Howard Hughes Medical Institute, Brandeis University, Waltham, MA, and approved February 27, 2017 (received for review December 10, 2016)

The calcium (Ca^{2+}) uniporter of mitochondria is a holocomplex consisting of the Ca^{2+}-conducting channel, known as mitochondrial calcium uniporter (MCU), and several accessory and regulatory components. A previous electrophysiology study found that the uniporter has high Ca^{2+} selectivity and conductance and this depends critically on the conserved amino acid sequence motif, DXXE (Asp-X-X-Glu) of MCU. A recent NMR structure of the MCU channel from *Caenorhabditis elegans* revealed that the DXXE forms two parallel carboxylate rings at the channel entrance that seem to serve as the ion selectivity filter, although direct ion interaction of this structural motif has not been addressed. Here, we use a paramagnetic probe, manganese (Mn^{2+}), to investigate ion and inhibitor binding of this putative selectivity filter. Our paramagnetic NMR data show that mutants with a single carboxylate ring, NXXE (Asn-X-X-Glu) and DXXQ (Asp-X-X-Gln), each can bind Mn^{2+} specifically, whereas in the WT the two rings bind Mn^{2+} cooperatively, resulting in ∼1,000-fold higher apparent affinity. Ca^{2+} can specifically displace the bound Mn^{2+} at the DXXE site in the channel. Furthermore, titrating the sample with the known channel inhibitor ruthenium 360 (Ru360) can displace Mn^{2+} binding from the solvent-accessible Asp site but not the inner Glu site. The NMR titration data, together with structural analysis of the DXXE motif and molecular dynamics simulation, indicate that the double carboxylate rings at the apex of the MCU pore constitute the ion selectivity filter and that Ru360 directly blocks ion entry into the filter by binding to the outer carboxylate ring.

MCU | calcium channel | selectivity filter | Ru360 binding | NMR

Calcium (Ca^{2+}) uptake by mitochondria is a long-known physiological phenomenon that is important for regulating various cellular activities such as aerobic metabolism and cell death (1–3). This uptake of Ca^{2+} is achieved by a Ca^{2+} uniporter whose activity can be blocked by ruthenium red (RuR) or ruthenium 360 (Ru360) (4). It was later shown by patch-clamping the inner mitochondrial membrane that this uniporter achieves remarkably high Ca^{2+} conductance and selectivity (5). Only about 5 y ago was the molecular identity of the channel component of the uniporter identified using integrative genomics approaches (6, 7). This channel is commonly referred to as the mitochondrial calcium uniporter (MCU). In metazoans, however, the uniporter is much more complex than just the pore-forming subunit; it is a holocomplex (also called a uniplex) containing other regulatory components. Among them, the single-pass transmembrane (TM) protein EMRE (Essential MCU REgulator) is absolutely required for the MCU to conduct ions (8). Two soluble components in the intermembrane space, MICU1 and MICU2, are Ca^{2+}-sensing proteins that gate the activity of MCU based on outside Ca^{2+} concentrations through EMRE (9–12). The current consensus is that the minimum requirements for uniporter-mediated Ca^{2+} flux in metazoans are MCU and EMRE, whereas in lower organisms such as *Dictyostelium* that lack EMRE, MCU is able to operate (13).

In an earlier study, we determined the pore architecture of the MCU channel using structural data obtained from solution NMR and negative-stain EM experiments (14). That structural study was performed on a *Caenorhabditis elegans* MCU construct with the N-terminal domain (NTD; residues 1–165) deleted, denoted as cMCU-ΔNTD. This protein construct has been shown to function as the full-length MCU in the mitochondrial Ca^{2+} uptake assay (14). The MCU is a homopentamer with the second TM helix forming a hydrophilic pore across the presumed lipid bilayer. The TM pentamer is further stabilized by a C-terminal domain that forms a coiled-coil pentamer outside the membrane. Perhaps the most interesting structural element is two parallel carboxylate rings formed by the Asp240-X-X-Glu243 (DXXE) motif at the entrance of the pore, on the intermembrane space side of the channel. For convenience, the conserved Asp240 and Glu243 are denoted here as D and E, respectively. The D ring is solvent-exposed and the E ring is located deeper inside the pore. Although NMR restraints were insufficient to provide the precise conformation of the carboxylate rings, the approximate dimensions of the D and E rings, as estimated based on the backbone Cβ positions, are 7 and 11 Å, respectively, which are consistent with specific cation binding (15–17). Moreover, functional mutagenesis showed that mutating either D or E causes MCU to lose channel activity nearly completely (6), providing further support for DXXE's role in recruiting and selecting ions.

In general, the selectivity filter is an important determinant of ion selectivity and conductivity of a channel (18, 19). The uniporter demonstrates very high Ca^{2+} conductance (i.e., a maximum reported flux of 5×10^6 Ca^{2+} s^{-1} at 105 mM Ca^{2+} and −160 mV voltage) (5). The uniporter is also strongly selective, with ∼10^3- to 10^6-fold higher selectivity for Ca^{2+} over Na^+ (5). Both conductance and selectivity of the uniporter are high compared with, for example, the Ca^{2+} release-activated Ca^{2+} channel Orai and the CorA Mg^{2+} channel. In the case of Orai, there is only one ring of six glutamate side chains at the pore entrance (17).

Significance

Mitochondrial calcium homeostasis is vital to cellular activities such as aerobic ATP production and cell death. Calcium uptake by mitochondria is achieved using an intricately regulated calcium channel, known as mitochondrial calcium uniporter (MCU). MCU demonstrates high calcium selectivity and conductance but little is known about its ion selectivity filter. We used paramagnetic NMR to show that the double carboxylate rings formed by the "DXXE" signature sequence of MCU is the ion selectivity filter and that the two ion binding sites can afford high ion affinity via positive cooperativity. We also showed that the channel inhibitor Ru360 directly blocks at the selectivity filter. Our approach demonstrates the promising application of NMR in investigating ion channels interacting with ions and blockers.

Author contributions: C.C., T.C., and J.J.C. designed research; C.C. and S.W. performed research; X.-C.S. contributed new reagents/analytic tools; C.C., S.W., X.-C.S., and J.J.C. analyzed data; and C.C., X.-C.S., and J.J.C. wrote the paper.

The authors declare no conflict of interest.

This article is a PNAS Direct Submission.

[1]To whom correspondence may be addressed. Email: xunchengsu@nankai.edu.cn or james_chou@hms.harvard.edu.

This article contains supporting information online at www.pnas.org/lookup/suppl/doi:10.1073/pnas.1620316114/-/DCSupplemental.

The CorA Mg^{2+} channel shows a pentameric selectivity ring but formed with Asn (15, 16). Moreover, Ru360 is a potent blocker of MCU conductance and has been suggested to bind to the apex of the channel according to mutagenesis studies (6, 20). It is not known whether Ru360 blocks Orai or CorA. Although previous functional studies established channel properties of MCU and the putative mechanism of Ru360 inhibition (5, 6, 14), structural information on ion and inhibitor binding is still missing.

In this study, to gain insights into understanding how MCU manages to achieve both high Ca^{2+} conductance and selectivity we focused on addressing whether the DXXE motif is capable of binding divalent cations, which is obviously a requirement of being the selectivity filter, and, if so, how it interacts with the ion in the double-ring configuration. While researchers await a high-resolution structure of the MCU bound to Ca^{2+}, we sought to capitalize on the NMR system developed for the cMCU-ΔNTD to address the above question. Because Ca^{2+} is not suitable for directly probing ion binding by NMR, we used paramagnetic manganese (Mn^{2+}), which is also a permeable divalent cation of MCU (5), to map residue-specific ion binding. We found that Mn^{2+} interacts with the DXXE motif in a highly specific manner and that the bound Mn^{2+} can be displaced with Ca^{2+}. By combining mutagenesis and paramagnetic NMR measurements we also found that the D and E carboxylate rings can bind Mn^{2+} in a cooperative manner and that Ru360 can only interact with the solvent-accessible D ring. Our results show that the double-ring structural element formed by DXXE is the ion selectivity filter of MCU and that Ru360 inhibits MCU activity by directly blocking this filter.

Results

Mn^{2+} Binds Specifically to the DXXE Motif, Which Can Be Displaced by Ca^{2+}. Equilibrium ion binding properties of channels have been extremely difficult to measure using common biophysical methods such as isothermal titration calorimetry unless it is done with extreme care and precision, as has been demonstrated by a previous study that measured K^+ binding constants of the K^+ channel (21). A favorable feature of NMR is the ability to provide residue-specific binding information. Calcium ion is NMR-invisible and its binding to protein can only be indirectly inferred by chemical shift changes. Fortunately, previous channel recording studies reported four different MCU-permeable divalent cations (Ca^{2+}, Sr^{2+}, Mn^{2+}, and Ba^{2+}) (5), among which Mn^{2+} is a commonly used paramagnetic probe in NMR studies of Ca^{2+} and Mg^{2+} binding proteins (22–24). In the case of MCU, Mn^{2+} is a relevant ion for investigating Ca^{2+} binding because (*i*) Mn^{2+} can be conducted by MCU, (*ii*) the Ca^{2+} current can be reduced by low concentrations of Mn^{2+} (5), indicating that Mn^{2+} competes with Ca^{2+} for binding at the ion selectivity site, and (*iii*) Mn^{2+} and Ca^{2+} are both divalent cations that have similar coordination numbers (25). We thus used Mn^{2+} as a paramagnetic probe and used an NMR titration experiment to map the binding site(s) of the divalent cation in MCU.

The NMR experiments were performed using uniformly [^{15}N, ^{13}C, ^{2}H]-labeled cMCU-ΔNTD, which was expressed in *Escherichia coli* and purified by nickel–nitrilotriacetic acid affinity, ion exchange, and size-exclusion chromatography using a previously established protocol (14) (*Materials and Methods* and Fig. S1). We titrated a 20 μM (pentamer) cMCU-ΔNTD sample with Mn^{2+} at concentrations ranging from 0–40 μM (*Materials and Methods*). At each Mn^{2+} concentration, residue-specific NMR signal reduction due to paramagnetic relaxation enhancement (PRE) caused by the Mn^{2+} was measured using the 2D ^{1}H-^{15}N transverse relaxation optimized spectroscopy (TROSY)–heteronuclear single-quantum correlation (HSQC) and the 3D HNCO that correlates the chemical shifts of backbone ^{1}H, ^{15}N, and ^{13}C nuclides. During the Mn^{2+} titration, the DXXE motif showed the most rapid peak intensity reduction, with almost complete disappearance of the peaks of D and E at 20 μM Mn^{2+} (Fig. 1*A*). The 3D HNCO allowed examination of all assigned residues of cMCU-ΔNTD (Fig. 1*B*) by resolving the peak overlaps in the 2D spectrum. The residue-specific PRE is defined here as the ratio between the peak heights in the presence (I) and absence (I_0) of Mn^{2+}. Our data show that the severely affected region with $I/I_0 \leq 0.2$ is exclusively the DXXE motif (Fig. 1 *C* and *D*). The residues with less significant PRE ($0.2 < I/I_0 \leq 0.5$) are mostly in the short loop between the DXXE and the first TM helix (Fig. 1*D*). To further resolve the paramagnetic effects on D and E, we plotted I/I_0 as a function of [Mn^{2+}], which shows that the PRE on D is stronger than on E (Fig. 1 *E* and *F*). The above results provide direct evidence of specific binding of a divalent cation to the DXXE structural element.

Upon saturating the DXXE with Mn^{2+} we examined whether Ca^{2+} can displace the bound Mn^{2+}, leading to the recovery of D and E NMR signals. The sample was then titrated with 10, 20, and

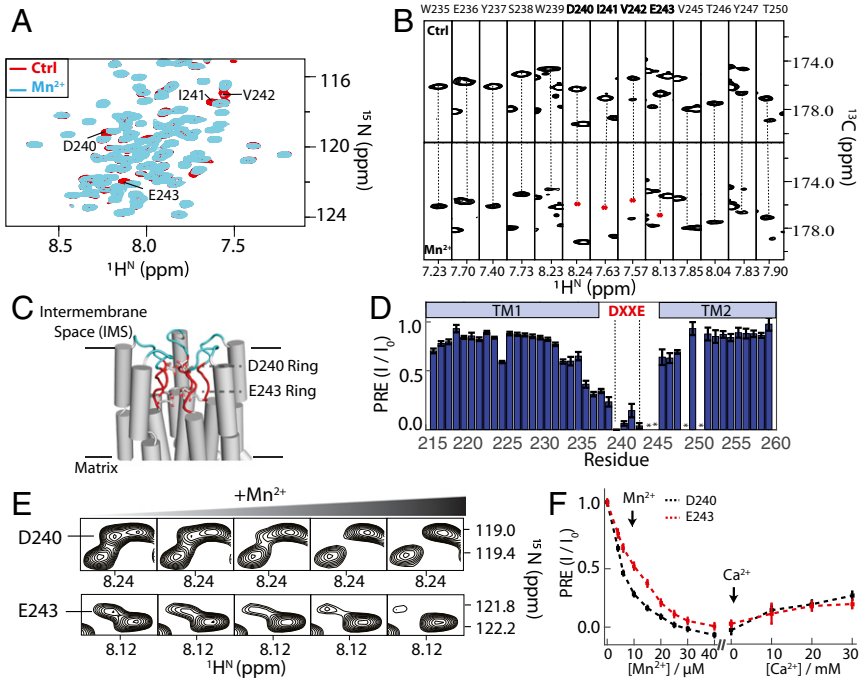

Fig. 1. Specific PRE of the WT DXXE motif induced by Mn^{2+}. (*A*) Superimposition of 2D ^{1}H-^{15}N TROSY-HSQC spectra of 20 μM (pentamer) U-[^{15}N, ^{13}C, ^{2}H] cMCU-ΔNTD without (red) and with (cyan) 40 μM Mn^{2+} shows that PRE effects of Mn^{2+} are localized in the DXXE motif. (*B*) Comparison of 3D TROSY-HNCO spectra of 20 μM (pentamer) U-[^{15}N, ^{13}C, ^{2}H] cMCU-ΔNTD before (*Top*) and after (*Bottom*) addition of 40 μM Mn^{2+}, showing the specific PREs of the DXXE motif in more resolved spectra. (*C*) Mapping the strong PREs ($I/I_0 \leq 0.5$) in *A* onto the cMCU-ΔNTD structure (red: $I/I_0 \leq 0.2$; cyan: $0.2 < I/I_0 \leq 0.5$). (*D*) Backbone amide PRE is plotted against residue number for the TM domain. The residues with overlap or without assignment are labeled with an asterisk. (*E*) The D240 and E243 peak intensities decrease with Mn^{2+} titration. The data were obtained from 2D ^{1}H-^{15}N TROSY-HSQC spectra with Mn^{2+} titrated into 20 μM (pentamer) cMCU-ΔNTD. (*F*) Plots of I/I_0 vs. [Mn^{2+}] for D240 (black) and E243 (red) of the WT cMCU-ΔNTD and recovery of I/I_0 upon addition of 10, 20, and 30 mM Ca^{2+}.

30 mM Ca^{2+}. At each Ca^{2+} concentration, 2D ^{1}H-^{15}N TROSY-HSQC and 3D TROSY-HNCO spectra were recorded. At 10 mM Ca^{2+}, we can see obvious peak recovery for D240 and E243 (Fig. S2). The peak intensities for D240 and E243 recovered to ∼20% at 30 mM Ca^{2+} concentration (Fig. 1*F*), above which the NMR sample became unstable. The inefficient displacement of Mn^{2+} by Ca^{2+} indicates that Ca^{2+} binding is much weaker than Mn^{2+}.

The Two Carboxylate Rings Can Bind Mn^{2+} Separately and Cooperatively. We next investigated whether each of the D and E carboxylate rings can specifically bind divalent cations. It is not possible to address this question by functional mutagenesis because mutating either D or E would almost completely abrogate channel activity (6, 7) and thus prohibit functional readout. We thus performed similar Mn^{2+} titration on the single carboxylate ring mutants including the D240N (or NXXE) and the E243Q (or DXXQ) mutants. These mutants were expressed and purified as was done for cMCU-ΔNTD. Size-exclusion profiles show that the mutants have the same oligomeric state as cMCU-ΔNTD (Fig. S3*A*). Moreover, the NMR spectra of the mutated and original cMCU-ΔNTDs are essentially the same except for perturbation of a few residues adjacent to the site of mutation, indicating that the mutations did not alter the channel conformation (Fig. S3*B*). We then performed Mn^{2+} titration on the mutants using titration protocols similar to that used for the cMCU-ΔNTD in Fig. 1.

The results show that the D peak of the DXXQ mutant and the E peak of the NXXE mutant are both sensitive to Mn^{2+} titration, although the rate of intensity reduction with respect to $[Mn^{2+}]$ is significantly lower than the corresponding rates of the WT DXXE (Fig. 2 *A* and *B*). The results indicate that the single carboxylate rings are capable of binding Mn^{2+}. We also found that the Q of the DXXQ mutant experienced much less paramagnetic effect compared with D (Fig. 2*C*), and the same is true for the N of the NXXE mutant (Fig. 2*D*), indicating that Mn^{2+} binding by D or E in the single-ring mutants is specific. At 40 μM Mn^{2+}, which caused saturation of PRE of D and E in DXXE, the D and E of the single-ring mutants showed 70% and 50% signal reduction, respectively (Fig. 2*E*). The complete PRE maps of the mutants are shown in Fig. S4. Overall, the results in Fig. 2 suggest that the single carboxylate ring is significantly weaker in recruiting Mn^{2+} than the double-ring WT.

To interpret the Mn^{2+} titration data more quantitatively, we estimated the apparent dissociation constant (K_d) using the PRE readouts. Because the channel concentration is not much lower than that of the ion, the simplified condition $[Mn^{2+}]_{total} \approx [Mn^{2+}]_{free}$ no longer holds. Hence, we simulated binding curves at a fixed channel concentration (20 μM) and a range of K_d values using the full analytical solution describing the fraction of ion-bound sites and estimated K_d by comparing the experimental data with the simulated curves. For the single-ring mutants, the analytical solution used was that for one binding site (Eq. **1** and Fig. S5). In terms of the observed PRE, the fraction of ion-bound sites is given by $1- I/I_0$. By identifying the simulated curve that agrees best with the experimental $(1- I/I_0)$ vs. $[Mn^{2+}]$ data, the apparent K_d could be estimated. Using such analysis, we found that the apparent K_d values for the single-ring mutants are ∼30 μM for the E ring and ∼10 μM for the D ring (Fig. 2*F*).

For the WT DXXE, the equilibrium binding equation used was that for two nonidentical binding sites (Eq. **2** and Fig. S5). By using the intrinsic K_d of the D and E sites obtained from the mutants, the

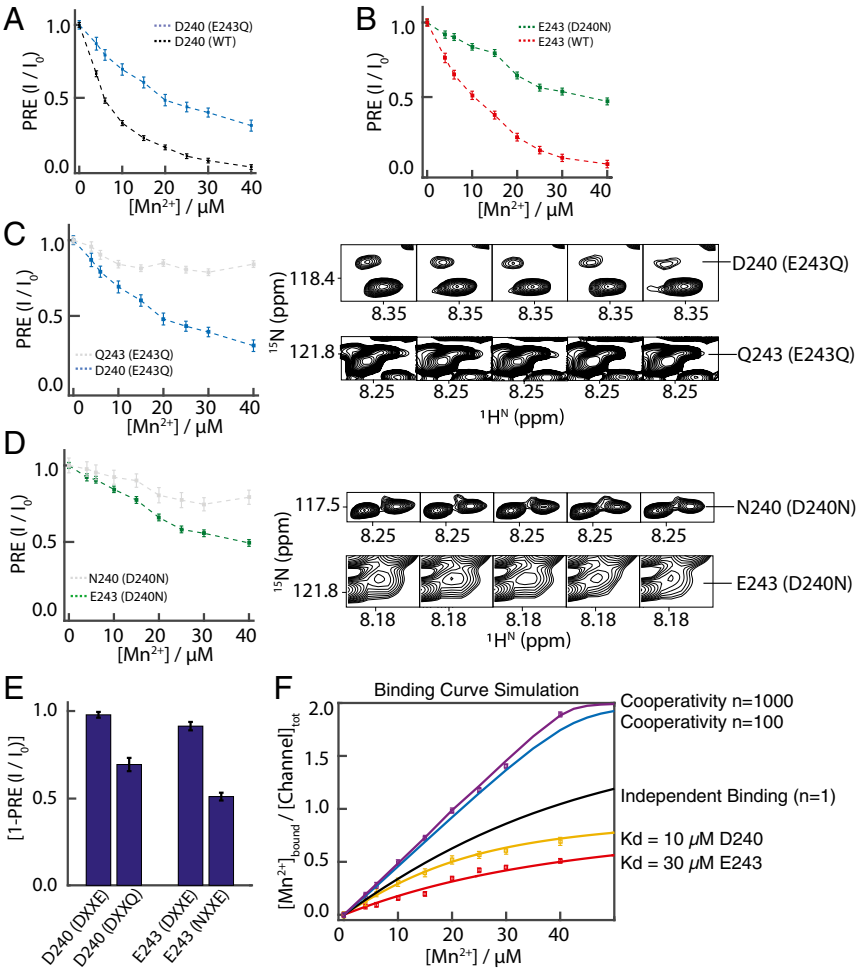

Fig. 2. PRE of the mutant DXXQ and NXXE motifs induced by Mn^{2+}. (*A*) PRE (I/I_0) vs. $[Mn^{2+}]$ plots for D240 in the WT DXXE (black) and the DXXQ mutant (blue). The channel concentration is 20 μM. (*B*) PRE vs. $[Mn^{2+}]$ plots for E243 in the WT DXXE (red) and the NXXE mutant (green). The channel concentration is 20 μM. (*C*) PRE vs. $[Mn^{2+}]$ plots for D240 (blue) and Q243 (gray) in the DXXQ mutant. (*D*) PRE vs. $[Mn^{2+}]$ plots for E243 (green) and N240 (gray) in the NXXE mutant. (*E*) At 40 μM Mn^{2+}, which caused PRE saturation of D and E in the WT DXXE, the D and E of the single-ring mutants showed 70% and 50% signal reduction, respectively. (*F*) Comparison between the PRE-derived $[Mn^{2+}]_{bound}$/[channel] and simulated binding curves for the one-site (Eq. **1**) and two-site (Eq. **2**) systems (*Materials and Methods*). For the one-site mutants, $[Mn^{2+}]_{Bound}$/[channel] (calculated as $1- I/I_0$) and simulated curves are shown for DXXQ (yellow) and NXXE (red). For the two-site WT, the $[Mn^{2+}]_{Bound}$/[channel] points were calculated using Eq. **3** (shown in purple). The two-site binding curves with $n = 1$ (no cooperativity), $n = 100$, and $n = 1{,}000$ are shown in black, blue, and purple, respectively.

two-site binding curves without and with cooperativity were simulated (Fig. 2*F*). Direct conversion of PRE data to $[Mn^{2+}]_{Bound}$/[channel] in the two-site case is, however, not straightforward due to cross-site PRE. For example, the sum of $1-I/I_0$ for D and E at 20 μM Mn^{2+} and 20 μM channel, which should be ≤1 (or one Mn^{2+} per channel), is around 1.6 (Fig. S6). The extra PRE is due to a cross-site effect because one ion can shuttle rapidly back and forth between the two sites to induce PRE at both sites. In addition, the cross-site PRE includes long-range PRE between the two sites. Therefore, $[Mn^{2+}]_{Bound}$/[channel] was calculated from the PRE data after subtracting the cross-site PRE as in Eq. **3** (*Materials and Methods*). Comparing experimentally derived $[Mn^{2+}]_{Bound}$/[channel] with the simulated curves showed that having two nearby but independent sites (cooperativity factor $n = 1$) cannot account for the increased sensitivity to Mn^{2+} relative to the one-site mutant (Fig. 2*F*). Cooperativity must be introduced to obtain close agreement with the experimental data, and a qualitative comparison suggests a cooperativity factor (n) around 1,000.

Ru360 Binds to the D but Not the E Site. Ru360, a linear dimer containing two octahedral ruthenium centers (Fig. 3*A*), is a potent inhibitor of mitochondrial Ca^{2+} uniporter (20). Earlier functional mutagenesis studies of the human MCU (HsMCU) showed that mutating S259 (S238 in cMCU) to Ala did not significantly affect MCU-mediated Ca^{2+} uptake but conferred resistance to Ru360 block (6). The NMR structure of the cMCU-ΔNTD shows that this serine (S238) is located at the apex of the pore adjacent to D240 (Fig. 3*B*), suggesting the possibility of Ru360's directly binding to the DXXE selectivity filter. Ru360 is not strongly paramagnetic and thus could not be used to directly induce PRE to map its binding site. It is nevertheless possible to test Ru360 binding to the D and E carboxylate rings by measuring Ru360 displacement of the bound Mn^{2+}.

We first tested whether Ru360 competes with Mn^{2+} in binding to the D ring. The DXXQ mutant was first titrated with Mn^{2+} up to a concentration of 20 μM, at which the peak intensity decreased by ~60% (Fig. 3 *C* and *D*). Then the sample was titrated with 0–1 mM Ru360. Increasing Ru360 concentration led to rapid recovery of the D peak intensity with an apparent K_d of ~100 μM (Fig. 3 *C* and *D*). We then tested Ru360 binding to the E site by performing the same titration experiment using the NXXE mutant. In this case, titrating Mn^{2+} up to 20 μM led to ~30% peak intensity reduction (Fig. 3 *E* and *F*). However, subsequent Ru360 titration did not recover the peak intensity (Fig. 3 *E* and *F*). These results indicate that Ru360 binds to the D ring but not to the E ring.

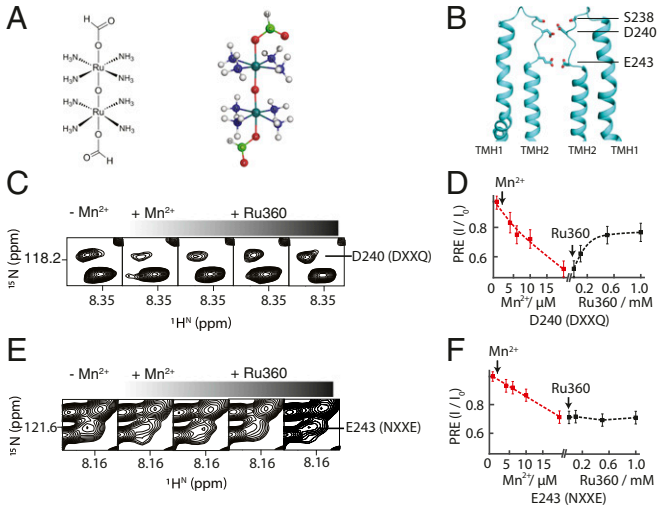

Fig. 3. The Ru360/Mn^{2+} replacement titration for the single-ring mutants. (*A*) The crystal structure of Ru360 showing a linear dimer containing two octahedral rutheniums linked by an oxygen bridge with the ends of the molecule capped with formates. (*B*) The cMCU-ΔNTD NMR structure showing that S238 is located at the apex of the pore adjacent to D240. (*C*) D240 peak intensity recovery by Ru360 titration at 0, 0.1, 0.5, and 1 mM. The mutant channel concentration used for Mn^{2+} and Ru360 titration is 20 μM. (*D*) The D240 recovery curve is shown as normalized peak intensity vs. [Ru360], in which the normalized peak intensity is defined as I (peak height at a given concentration of Ru360)/I_0 (peak height without Mn^{2+} or Ru360). (*E*) The E243 peak recovery by Ru360 titration at 0, 0.1, 0.5, and 1 mM. (*F*) The E243 recovery curve as in *C* but shows no peak recovery.

It is still possible, however, that Ru360 binds to a site near the D ring and causes the D ring to lose Mn^{2+} affinity via allosteric mechanism. We thus carried out further molecular dynamics (MD) simulation to examine whether direct Ru360 binding to the D ring is energetically favorable. The MD simulation system consists of the cMCU-ΔNTD structure and Ru360 embedded in 1-palmitoyl-2-oleoyl-*sn*-glycero-3-phospcholine (POPC) lipid bilayer (*Materials and Methods*). Ru360 was vertically placed along the fivefold axis near the channel apex at the beginning of the simulation. After ~25 ns of simulation, the system reached equilibrium and Ru360 indeed bound stably at the channel entrance, showing ~45° tilt angle relative to the channel axis and extensive contacts with the D ring (Fig. 4 *A* and *B*). The amine groups of Ru360 interact strongly with side-chain carboxylate and backbone oxygen atoms of D by forming hydrogen-bonding meshwork (Fig. 4*C*). In addition, the amino groups of Ru360 showed interaction with S238 (Fig. 4*C*). The simulation did not suggest any Ru360 interactions with E243.

Discussion

We have shown highly specific binding of Mn^{2+} to the pentameric carboxylate rings formed by the DXXE motif of MCU. We have also shown that each of the rings formed by D and E alone is capable of binding Mn^{2+}, although at much weaker apparent affinity. The observed interactions between Mn^{2+} and the carboxylate rings are also selective because there are many accessible clusters of acidic residues in the protein but only those of the DXXE motif showed strong PRE at low Mn^{2+} concentration (DXXE resonances essentially disappeared at 1:1 channel:ion ratio). Moreover, because the bound Mn^{2+} can be specifically displaced by Ca^{2+}, the reported Mn^{2+} binding to the DXXE carboxylate rings should hold for Ca^{2+}, except the binding affinity and cooperativity are likely different according to the different conductance (5).

Based on previous functional mutagenesis of DXXE and the direct proof of DXXE's binding to a divalent cation reported in this study we can now more confidently assign the DXXE motif as the MCU ion selectivity filter and elucidate its structure in the context of ion selectivity and conductance. On a first look at the DXXE structure, the solvent-accessible D ring resembles strongly to the pentameric N ring of the CorA Mg^{2+} channel and the hexameric E ring of the Orai Ca^{2+} channel. Orai is considered as highly selective for Ca^{2+} (half-maximal block of monovalent current at ~10 μM Ca^{2+}) but having rather modest conductivity (up to 10^4 ions per second) (26–29). The pore structure of Orai suggests that the selectivity filter is a single ring of glutamates, which is compatible with a single high-affinity Ca^{2+} binding site with a fast on-rate and a slow off-rate (17). For the CorA channel, the pentameric N ring is directly involved in coordinating Mg^{2+}, although in the absence of Mg^{2+} the channel is nonselective and permeable to cations (30).

The NMR structural and titration data show that both D and E rings can bind Mn^{2+} separately and they are aligned in parallel uniaxial configuration. The multiple ion binding sites along the pore axis is reminiscent of the selectivity filter of the tetrameric K^+ channels, and thus comparison with the high-resolution structure of KcsA ought to be informative for understanding the high ion selectivity and conductance. The KcsA channel has 10,000-fold higher selectivity for K^+ over Na^+ and a conductance of 10^8 K^+ ions per s (close to the diffusion limit) (19); it is a textbook example of an ion channel having both high selectivity and high conductivity (31). The selectivity filter of KcsA is formed by four equivalent signature sequences (TVGYG) in extended conformation. The backbone carbonyl oxygen atoms of

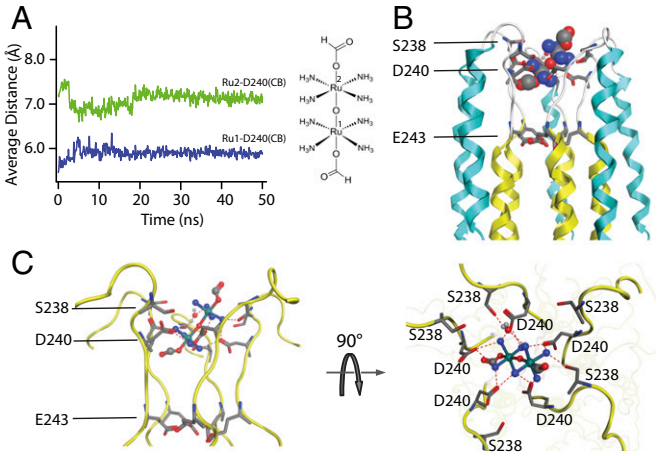

Fig. 4. MD simulation of Ru360 binding to the MCU pore. (*A*) The distances between the ruthenium centers of Ru360 and the β carbons of D240 (averaged over the five protomers) vs. simulation time. (*B*) The average Ru360 position relative to the cMCU-ΔNTD NMR structure showing the overall location of the inhibitor. (*C*) Zoomed side and top views of Ru360 interacting with D240 of the DXXE selectivity filter, showing possible hydrogen bonds between MCU and Ru360 (dashed lines).

VGYG are aligned toward the center of the filter pore, forming four parallel squares (labeled S1–S4 from the extracelleular side) capable of coordinating K^+ or water molecules (19).

In one of the proposed ion coordination models for KcsA, two K^+ ions can be coordinated either at the S1 and S3 sites or at the S2 and S4 sites, with water molecules bound to the alternate sites between the two K^+ ions (Fig. 5*A*) (32, 33). In the high-resolution crystal structures, the distance between the two K^+ ions is ∼7.5 Å (19, 32). Based on the structural finding, it has been suggested that a single K^+ ion could be held very tightly (21), but that the presence of two K^+ ions in close proximity results in mutual repulsion, which enables fast ion conduction by exploiting electrostatic repulsive forces (19). A similar mechanism could explain the fast Ca^{2+} conduction by the MCU because the average distance between the D and E rings in the NMR structure ensemble is 8.0 Å with ∼1.5 Å uncertainty (Fig. 5*B*), consistent with the separation between the K^+ binding sites S1 and S3 or S2 and S4 in KcsA. We thus propose that each of the two pentameric rings formed by DXXE serves as an ion-binding center, and that two bound Ca^{2+} are separated by ∼8 Å in the selectivity pore and are likely bridged by an intervening water molecule as in the KcsA.

The pentagonal bipyramid coordination arrangement could also explain high selectivity and would agree well with the coordination number of seven for Ca^{2+}, because five oxygen atoms of the D or E ring coordinate ions in a plane while water molecules on the two sides of the plane interact with the ion along the pore axis (Fig. 5*C*). The pentagonal bipyramid conformation is common for Ca^{2+}-binding proteins (Fig. S7), for example, the canonical EF-hand motif, the HRV (rhinovirus) protein (34, 35), and the Ca^{2+} ATPase (36). Ion selectivity is the result of highly specific ion binding to the permeation pathway (18), and we propose that the double carboxylate rings of MCU generate strong ion affinity through positive cooperativity. Although the NMR titration method is only suitable for measuring micromolar K_d values, comparing the Mn^{2+} titrating data with simulations suggests that the upper limit of apparent K_d is ∼10 nM, which is three orders of magnitude larger than the 10 and 30 μM K_d values for the individual D and E rings, respectively. Indeed, such cooperativity is expected in the pentagonal bipyramid coordination model, in which the two ions are bridged by interactions with the same water molecule. The strong Mn^{2+} binding is also consistent with the very slow Mn^{2+} flux reported by previous patch-clamp experiments (5).

The binding of Ru360 to the apex of the MCU pore has already been suggested based on the mutagenesis of S259 in human (6) and S238 in *C. elegans* (14). In the cMCU structure, S238 is adjacent to the D ring, and its hydroxyl group possibly interacts with the amine groups of Ru360 (Fig. 4*A*). Our Ru360 titration data of the single-ring mutants show that Ru360 displaces Mn^{2+} at the D ring but not at the E ring, suggesting that Ru360 interacts with the negatively charged D ring. Therefore, Ru360–MCU complex should be mediated by electrostatic and hydrogen-bonding interactions between the Ru360 amine groups and the electronegative carboxylate groups of D240 and the hydroxyl group of S238, as suggested by the MD simulation (Fig. 4*C*). In addition to the polar contacts, size and shape complementarily also seemed important because the diameter of the Ru360 allows a snug fit of the compound to the hollow at the channel apex (Fig. S8).

In summary, we provide direct evidence of specific binding of a divalent cation to the conserved DXXE motif of MCU and show that ion binding to the aspartate and glutamate rings is cooperative. The NMR titration data together strongly indicate that the DXXE motif forms the Ca^{2+} selectivity filter of MCU, similar to the K^+ selectivity filter of the KcsA channel. It was not clear whether the Ser-to-Ala mutations near the pore entrance (S259A in human and S238A in *C. elegans*) confer resistance to Ru360 blocking via allosteric mechanism or direct abrogation of Ru360 binding at the pore entrance. Our Ru360/Mn^{2+} displacement data show that Ru360 directly binds to the solvent-accessible aspartate ring formed by the DXXE motif. Therefore, Ru360 inhibits the channel by directly blocking the entrance to the selectivity pore. The NMR titrations were all performed in the absence of the channel activator EMRE, and thus the channel under study is presumably in a state that can bind but not conduct divalent cations. A recent study suggests that EMRE may directly interact with the TM domain of MCU (37). Hence, the effect of EMRE on ion binding to the selectivity filter, if any, remains to be investigated.

Materials and Methods

Protein Expression and Purification. *E. coli*-codon optimized DNA encoding residues 167–316 of the *C. elegans* MCU (cMCU-ΔNTD) with C-terminal 6-His tag was expressed and purified as described previously (14). The final NMR sample for 2D ^{1}H-^{15}N TROSY-HSQC spectra contains 20μM cMCU-ΔNTD (pentamer) in 20 mM MES, pH 6.4, 75 mM NaCl, ∼1 mM foscholine-14, 0.3 mM NaN_3, and 5% (vol/vol) D_2O. The mutants D240N and E243Q samples were prepared with the same way as for the original cMCU-ΔNTD.

NMR Titration Experiments. All NMR titration experiments were performed on a 750-MHz Bruker spectrometer equipped with cryogenic probe at 306 K. Uniformly (^{15}N, ^{13}C, 85% ^{2}H)-labeled cMCU-ΔNTD and its mutants at 20 μM concentration (pentamer) were used for titration. $MnCl_2$ stock solution was added to 300 μL protein sample to reach final concentrations of 4, 6, 10, 15, 20, 25, 30, and 40 μM. For Ru360 titration, 0.1, 0.5, and 1 mM Ru360 was added in the same manner. At each ligand concentration point, 2D ^{1}H-^{15}N TROSY-HSQC and 3D TROSY-HNCO spectra were recorded. The spectra were processed using NMRPipe and analyzed using Sparky.

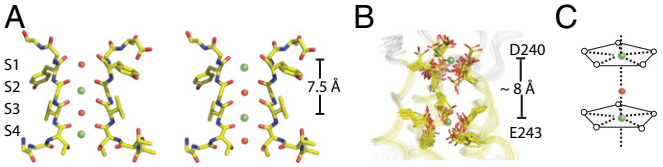

Fig. 5. Proposed model for Ca^{2+} binding to the MCU selectivity filter. (*A*) Coordination of K^+ ions either at the S1 and S3 sites or at the S2 and S4 sites, with water molecules (red sphere) bound to the alternate sites between the two K^+ ions (green sphere). The distance between the two K^+ ions is 7.5 Å [atomic coordinates from Protein Data Bank (PDB) ID code 1BL8]. (*B*) The NMR structure ensemble of the DXXE motif showing the average distance between the D and E rings is 8.0 ± 1.5 Å (atomic coordinates from PDB ID code 5ID3). The green spheres represent hypothetical ions bound at the two ring positions. (*C*) The proposed Ca^{2+} pentagonal bipyramid coordination as five oxygen atoms of D or E ring coordinate ion in a plane while water molecules on the two sides of the plane interact with the ion along the pore axis.

MD Simulations. MD simulations were performed using the Desmond 4.5 package. The OPLS-AA 2005 force field in a neutral POPC bilayer with appropriate number of counter ions was used to balance the net charge of the system solvated in 0.15 M NaCl. The cMCU-ΔNTD channel structure, Ru360, and POPC bilayer were embedded in a periodic orthorhombic box (~14 × 14 × 14 Å^3) containing the explicit simple point charge (SPC) water molecules, which ensured that the surfaces of the MCU and Ru360 were covered by bilayer and/or water molecules. MD simulations were carried out for 50 ns with the periodic boundary conditions in the NPT ensemble [in which the amount of substance (N), pressure (P) and temperature (T) were conserved].

One-Site and Two-Site Binding Models. The general solution of one-site binding used for simulating binding curves in Fig. 2*F* is

$$\frac{S_B}{P_T}=\frac{(P_T+S_T+K_d)\pm\sqrt{(P_T+S_T+K_d)^2-4P_TS_T}}{2P_T}, \quad [1]$$

where P_T and S_T are the total channel and Mn^{2+} concentrations, respectively, and S_B is the concentration of bound Mn^{2+}.

The general solution of two-site binding with cooperativity included is

$$nK_1K_2S_B^3+\left(-K_1-K_2-2nK_1K_2S_T^2-2nK_1K_2P_T^2\right)S_B^2+\left[1+(K_1+K_2)S_T+nK_1K_2S_T^2 +(K_1+K_2)P_T+4nK_1K_2S_TP_T\right]S_B+\left[-(K_1+K_2)S_T-2nK_1K_2S_T^2\right]P_T=0, \quad [2]$$

where P_T, S_T, *and* S_B are defined as above, K_1 and K_2 are binding constants for the E and D binding sites, respectively, and n is the cooperativity factor. Derivations are given in *SI Materials and Methods*.

Converting PRE Data to Population of Bound Mn^{2+}. For the two-site case, the number of bound Mn^{2+} per channel, $[Mn^{2+}]_{Bound}$/[channel], is the sum of (1 – PRE) for the D site and (1 – PRE) for the E site subtracting the contribution from cross-site PRE. The cross-site PRE is introduced when a bound Mn^{2+} (at one site in a channel) can hop to an unbound site within the same channel, and this is given by the product of the number of bound Mn^{2+} per channel and the probability of having an unbound site in the channel (2[channel] – $[Mn^{2+}]$)/(2[channel]). In addition, the cross-site PRE includes long-range PRE between the two sites, and this can be estimated similarly as in the case of ion hopping except it is much weaker because the intersite PRE distances are substantially longer than the intrasite PRE distances. Combining the above yields

$$\frac{[Mn^{2+}]_{Bound}}{[channel]}=(2-PRE_D-PRE_E)-(1+X)\frac{[Mn^{2+}]_{Bound}}{[channel]}\left(\frac{2[channel]-[Mn^{2+}]}{2[channel]}\right), \quad 0\le[Mn^{2+}]\le 2[channel], \quad [3]$$

where PRE_D and PRE_E are the I/I_0 measured for the D and E resonance, respectively, at each of the titration points and X is the ratio of the intersite PRE to the intrasite PRE, observed for the DXXQ and NXXE mutants in Fig. 2 *C* and *D* at each of the Mn^{2+} concentrations.

ACKNOWLEDGMENTS. We thank Vamsi K. Mootha and his group for insightful discussions and critical reading of our paper. We thank the Harvard Center for Molecular Interaction for helping with isothermal titration calorimetry and size exclusion chromatography coupled to multiple-angle light-scattering experiments. The NMR data were collected at the NMR facility of MIT-Harvard Center for Magnetic Resonance (supported by NIH Grant P41 EB-002026) and National Center for Protein Science Shanghai of the Chinese Academy of Sciences (CAS). This work was supported by CAS Grant XDB08030301, NIH Grants GM116898 and HL130143 (to J.J.C.), Major National Scientific Research Project 2013CB910201, and National Science Foundation of China Grant 21473095 (to X.-C.S.). C.C. is supported by the China Scholarship Council.

1. Deluca HF, Engstrom GW (1961) Calcium uptake by rat kidney mitochondria. *Proc Natl Acad Sci USA* 47(11):1744–1750.
2. Vasington FD, Murphy JV (1962) Ca ion uptake by rat kidney mitochondria and its dependence on respiration and phosphorylation. *J Biol Chem* 237(13925019):2670–2677.
3. Denton RM, McCormack JG (1980) The role of calcium in the regulation of mitochondrial metabolism. *Biochem Soc Trans* 8(3):266–268.
4. Gunter TE, Pfeiffer DR (1990) Mechanisms by which mitochondria transport calcium. *Am J Physiol* 258(5 Pt 1):C755–C786.
5. Kirichok Y, Krapivinsky G, Clapham DE (2004) The mitochondrial calcium uniporter is a highly selective ion channel. *Nature* 427(6972):360–364.
6. Baughman JM, et al. (2011) Integrative genomics identifies MCU as an essential component of the mitochondrial calcium uniporter. *Nature* 476(7360):341–345.
7. De Stefani D, Raffaello A, Teardo E, Szabò I, Rizzuto R (2011) A forty-kilodalton protein of the inner membrane is the mitochondrial calcium uniporter. *Nature* 476(7360):336–340.
8. Sancak Y, et al. (2013) EMRE is an essential component of the mitochondrial calcium uniporter complex. *Science* 342(6164):1379–1382.
9. Perocchi F, et al. (2010) MICU1 encodes a mitochondrial EF hand protein required for Ca(2+) uptake. *Nature* 467(7313):291–296.
10. Mallilankaraman K, et al. (2012) MICU1 is an essential gatekeeper for MCU-mediated mitochondrial Ca(2+) uptake that regulates cell survival. *Cell* 151(3):630–644.
11. Plovanich M, et al. (2013) MICU2, a paralog of MICU1, resides within the mitochondrial uniporter complex to regulate calcium handling. *PLoS One* 8(2):e55785–e55785.
12. Kamer KJ, Mootha VK (2015) The molecular era of the mitochondrial calcium uniporter. *Nat Rev Mol Cell Biol* 16(9):545–553.
13. Kovács-Bogdán E, et al. (2014) Reconstitution of the mitochondrial calcium uniporter in yeast. *Proc Natl Acad Sci USA* 111(24):8985–8990.
14. Oxenoid K, et al. (2016) Architecture of the mitochondrial calcium uniporter. *Nature* 533(7602):269–273.
15. Eshaghi S, et al. (2006) Crystal structure of a divalent metal ion transporter CorA at 2.9 angstrom resolution. *Science* 313(5785):354–357.
16. Lunin VV, et al. (2006) Crystal structure of the CorA Mg2+ transporter. *Nature* 440(7085):833–837.
17. Hou X, Pedi L, Diver MM, Long SB (2012) Crystal structure of the calcium release-activated calcium channel Orai. *Science* 338(6112):1308–1313.
18. Gouaux E, Mackinnon R (2005) Principles of selective ion transport in channels and pumps. *Science* 310(5753):1461–1465.
19. Doyle DA, et al. (1998) The structure of the potassium channel: Molecular basis of K+ conduction and selectivity. *Science* 280(5360):69–77.
20. Ying WL, Emerson J, Clarke MJ, Sanadi DR (1991) Inhibition of mitochondrial calcium ion transport by an oxo-bridged dinuclear ruthenium ammine complex. *Biochemistry* 30(20):4949–4952.
21. Liu S, et al. (2015) Ion-binding properties of a K+ channel selectivity filter in different conformations. *Proc Natl Acad Sci USA* 112(49):15096–15100.
22. Run C, Yang Q, Liu Z, OuYang B, Chou JJ (2015) Molecular basis of MgATP selectivity of the mitochondrial SCaMC carrier. *Structure* 23(8):1394–1403.
23. Grisham CM (1980) Paramagnetic probes in NMR and EPR studies of membrane enzymes. *J Biochem Biophys Methods* 3(1):39–59.
24. Koehler J, Meiler J (2011) Expanding the utility of NMR restraints with paramagnetic compounds: Background and practical aspects. *Prog Nucl Magn Reson Spectrosc* 59(4):360–389.
25. Harding MM (2001) Geometry of metal-ligand interactions in proteins. *Acta Crystallogr D Biol Crystallogr* 57(Pt 3):401–411.
26. Bakowski D, Parekh AB (2002) Monovalent cation permeability and Ca(2+) block of the store-operated Ca(2+) current I(CRAC)in rat basophilic leukemia cells. *Pflugers Arch* 443(5-6):892–902.
27. Chaudhuri D, Clapham DE (2014) Outstanding questions regarding the permeation, selectivity, and regulation of the mitochondrial calcium uniporter. *Biochem Biophys Res Commun* 449(4):367–369.
28. Prakriya M, Lewis RS (2006) Regulation of CRAC channel activity by recruitment of silent channels to a high open-probability gating mode. *J Gen Physiol* 128(3):373–386.
29. Zweifach A, Lewis RS (1993) Mitogen-regulated Ca2+ current of T lymphocytes is activated by depletion of intracellular Ca2+ stores. *Proc Natl Acad Sci USA* 90(13):6295–6299.
30. Dalmas O, et al. (2014) A repulsion mechanism explains magnesium permeation and selectivity in CorA. *Proc Natl Acad Sci USA* 111(8):3002–3007.
31. Roux B (2005) Ion conduction and selectivity in K(+) channels. *Annu Rev Biophys Biomol Struct* 34:153–171.
32. Zhou Y, Morais-Cabral JH, Kaufman A, MacKinnon R (2001) Chemistry of ion coordination and hydration revealed by a K+ channel-Fab complex at 2.0 A resolution. *Nature* 414(6859):43–48.
33. Ye S, Li Y, Jiang Y (2010) Novel insights into K+ selectivity from high-resolution structures of an open K+ channel pore. *Nat Struct Mol Biol* 17(8):1019–1023.
34. Zhao R, et al. (1996) Human rhinovirus 3 at 3.0 A resolution. *Structure* 4(10):1205–1220.
35. Zhao R, Hadfield AT, Kremer MJ, Rossmann MG (1997) Cations in human rhinoviruses. *Virology* 227(1):13–23.
36. Toyoshima C, Nakasako M, Nomura H, Ogawa H (2000) Crystal structure of the calcium pump of sarcoplasmic reticulum at 2.6 A resolution. *Nature* 405(6787):647–655.
37. Tsai MF, et al. (2016) Dual functions of a small regulatory subunit in the mitochondrial calcium uniporter complex. *eLife* 5:5.
38. Hoover WG (1985) Canonical dynamics: Equilibrium phase-space distributions. *Phys Rev A Gen Phys* 31(3):1695–1697.
39. Martyna GJ (1994) Remarks on "Constant-temperature molecular dynamics with momentum conservation". *Phys Rev E Stat Phys Plasmas Fluids Relat Interdiscip Topics* 50(4):3234–3236.
40. Hoover WG, Ciccotti G, Paolini G, Massobrio C (1985) Lennard-Jones triple-point conductivity via weak external fields: Additional calculations. *Phys Rev A Gen Phys* 32(6):3765–3767.
41. Cerutti DS, Duke RE, Darden TA, Lybrand TP (2009) Staggered Mesh Ewald: An extension of the Smooth Particle-Mesh Ewald method adding great versatility. *J Chem Theory Comput* 5(9):2322.
42. Shan Y, Klepeis JL, Eastwood MP, Dror RO, Shaw DE (2005) Gaussian split Ewald: A fast Ewald mesh method for molecular simulation. *J Chem Phys* 122(5):54101.
43. Deng Z, Martyna GJ, Klein ML (1992) Structure and dynamics of bipolarons in liquid ammonia. *Phys Rev Lett* 68(16):2496–2499.